



OCEANOGRAPHY

The 2023 extreme coastal El Niño: Atmospheric and air-sea coupling mechanisms

Qihua Peng¹, Shang-Ping Xie^{1*}, Gino A. Passalacqua², Ayumu Miyamoto¹, Clara Deser³

In the boreal spring of 2023, an extreme coastal El Niño struck the coastal regions of Peru and Ecuador, causing devastating rainfalls, flooding, and record dengue outbreaks. Observations and ocean model experiments reveal that northerly alongshore winds and westerly wind anomalies in the eastern equatorial Pacific, initially associated with a record-strong Madden-Julian Oscillation and cyclonic disturbance off Peru in March, drove the coastal warming through suppressed coastal upwelling and downwelling Kelvin waves. Atmospheric model simulations indicate that the coastal warming in turn favors the observed wind anomalies over the far eastern tropical Pacific by triggering atmospheric deep convection. This implies a positive feedback between the coastal warming and the winds, which further amplifies the coastal warming. In May, the seasonal background cooling precludes deep convection and the coastal Bjerknes feedback, leading to the weakening of the coastal El Niño. This coastal El Niño is rare but predictable at 1 month lead, which is useful to protect lives and properties.

INTRODUCTION

Because of the strong upwelling of cold subsurface water, deep convection is largely suppressed off Peru. Consequently, the Peruvian coastal region receives merely ~5 cm of annual rainfall (1), rendering it one of the driest places on Earth. In March–April 2023, an extreme coastal warming event, one of the strongest in the past four decades (figs. S1 and S2), occurred along the coast of Peru and Ecuador. This extreme coastal El Niño caused widespread flooding and the worst recorded dengue outbreak in Peruvian history, leading to more than 300 deaths (2, 3). The arid Sechura desert in northern Peru was submerged under a vast lake known as Lake La Niña, a phenomenon observed only during extreme El Niño events. Tens of thousands of homes were destroyed by the flooding. In addition, this event caused the lowest chlorophyll-a (Chl-a) concentrations in the coastal regions since the Moderate Resolution Imaging Spectroradiometer (MODIS) satellite measurements began in 2002 (fig. S3), with impacts on marine ecosystems and fisheries (4).

This type of phenomenon, distinguished by its distinct evolution, spatial pattern, dynamics, and impacts from basin-scale El Niño events, is categorized as a coastal El Niño (5–7). Similar extreme events occurred in 1925 (7) and 2017 (6, 8, 9). Some studies show that intraseasonal downwelling Kelvin waves (6, 10, 11) trigger the coastal El Niño, and coastal Bjerknes feedback (6) further amplifies it. Other studies suggest that surface heat flux anomalies (9), reduced atmospheric stability due to central Pacific cooling (7), or extratropical circulation anomalies in the Southern Hemisphere (8, 12) play an important role in driving the coastal El Niño. However, the rarity of extreme coastal El Niño events in modern instrumental records hinders a comprehensive understanding of the ocean-atmosphere dynamics involved. The occurrence of the 2023 coastal El Niño event, with extensive observations (some in real-time), presents a valuable opportunity to further investigate crucial dynamical processes of coastal El Niño. The 2023 event exhibits several unique features including unusual atmospheric perturbations in

the far eastern Pacific and strong subsurface temperature anomalies along the equator that leads to the rapid growth of a basin-scale El Niño. These features highlight the need for a close look into ocean-atmospheric processes that produced the 2023 coastal El Niño.

Here, we examine the evolution and mechanisms of the 2023 extreme coastal El Niño by using a variety of observations. We further use comprehensive ocean (OGCM) and atmospheric (AGCM) general circulation models to reveal the underlying oceanic and atmospheric dynamics. In addition to confirming the coastal Bjerknes feedback that amplifies the coastal El Niño, our results indicate that atmospheric internal variability in the far eastern Pacific helps trigger, and is also amplified by, the extreme coastal El Niño. Both observations and numerical experiments reveal that the seasonal cooling of background sea surface temperature (SST) decouples the coastal ocean and atmosphere from May onward, ultimately leading to the decay of the coastal El Niño.

RESULTS

Evolution of the 2023 coastal El Niño

The year of 2023 opened with the tropical Pacific Ocean in a La Niña state. The onset of the coastal warming was first observed in mid-February: Weak warming signals initially manifested in locations away from the coastline together with weak northwesterly winds over the equatorial southeastern Pacific Ocean (Fig. 1 and fig. S4). In early March, a burst of westerly wind anomalies took place in the eastern equatorial Pacific (EEP) (Fig. 2A), concomitant with strong northerly wind anomalies off Ecuador and Peru (Fig. 2D). The SST warming signal shifted to coastal regions and greatly intensified through March and April (Fig. 2C). The coastal El Niño peaked at the end of April with a monthly maximum SST anomaly of +4°C in the Coastal region of South America (CSA; averaged over 85°W to 80°W, 10°S to 0°), while the central equatorial Pacific sustained neutral conditions during this period. Monthly coastal SST warming in 2023 was the strongest at most coastal stations since 2000 (fig. S2), comparable to the extreme warming in 1983 and 1998 (fig. S1A). Positive sea level anomalies (SLA) exceeding 10 cm were observed along the equator and CSA (Fig. 2C and fig. S4B), coinciding with strong subsurface warming (exceeding 5°C) above 80 m in the

¹Scripps Institution of Oceanography, University of California San Diego, La Jolla, CA 92093, USA. ²Save The Waves Coalition, Santa Cruz, CA 95060, USA. ³National Center for Atmospheric Research, Boulder, CO, USA.

*Corresponding author. Email: sxie@ucsd.edu

Copyright © 2024 the Authors, some rights reserved; exclusive licensee American Association for the Advancement of Science. No claim to original U.S. Government Works. Distributed under a Creative Commons Attribution NonCommercial License 4.0 (CC BY-NC).

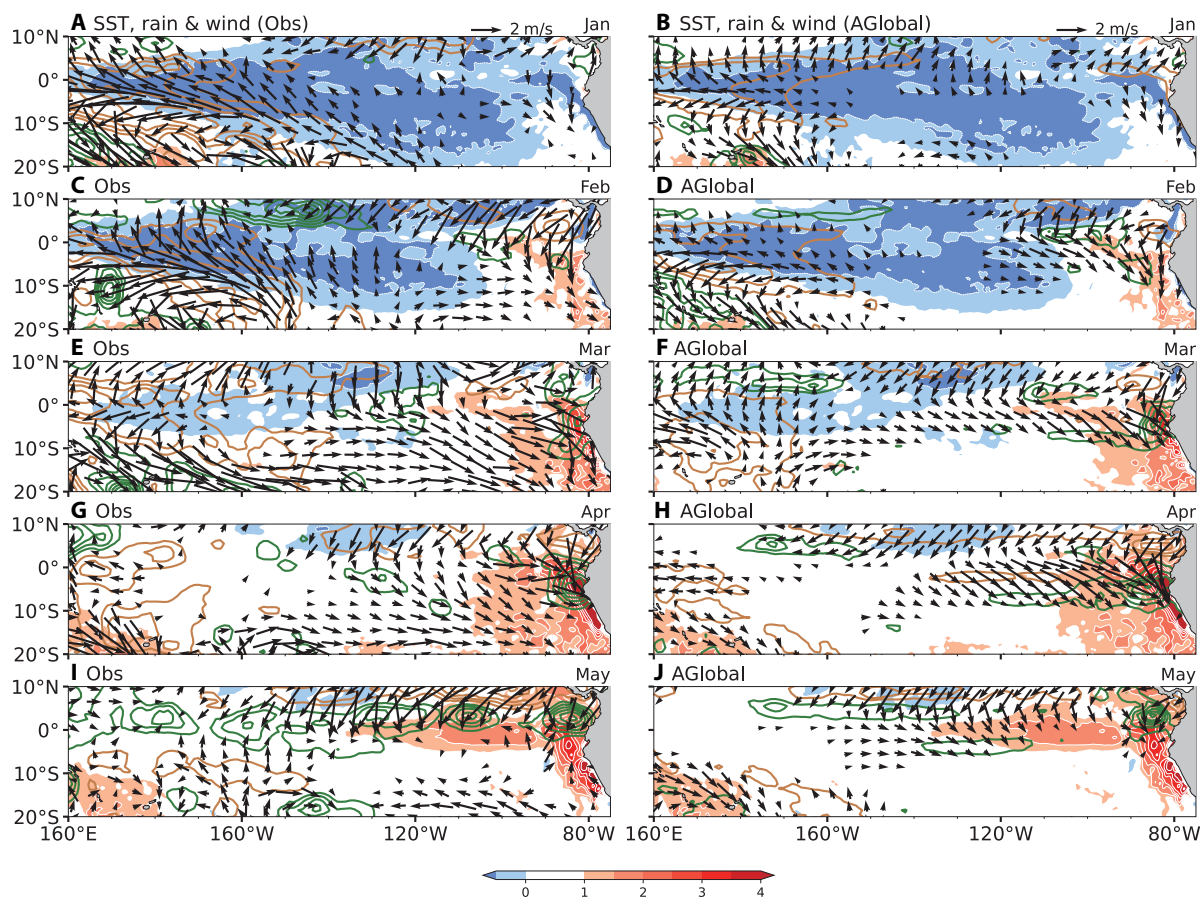


Fig. 1. The spatiotemporal distribution of the 2023 coastal El Niño and associated atmospheric conditions. Left: Observed SST ($^{\circ}\text{C}$, color shading), 10-m wind (meters per second, vectors; values below 0.5 m/s not shown), and rainfall anomalies (line contours with an interval of 2 mm/day; positive values in green and negative values in brown) during (A) January, (C) February, (E) March, (G) April, and (I) May. Right: Same as left but for the anomalous wind and rainfall obtained from the AGlobal experiment during (B) January, (D) February, (F) March, (H) April, and (J) May (see Materials and Methods for details).

coastal region (fig. S5). During this period, the coastal warming was accompanied by heavy rainfall (Figs. 1 and 2D) and the strongest 10-m meridional wind (v_{10}) anomalies off Peru since 1982 (fig. S1B).

The warming signals started to decay in May. The alongshore winds relaxed to their climatological state, accompanied by a return to normal rainfall amounts (Fig. 2 and fig. S4). In June, a basin-scale El Niño emerged, with westerly wind anomalies over the central-western equatorial Pacific. This evolution evokes similarities with the Rasmusson and Carpenter (RC) El Niño composite (13), which has been rarely observed during the satellite era. During the 1950s and the mid-1970s, warm SST anomalies first appeared off the coast of South America and then developed westward into basin-scale El Niños (13). After the 1976–1977 climate regime shift, this pattern reversed, with coastal warming often trailing the basin-wide peak (e.g., 1983 and 1998) (fig. S1A). This change coincides with a reversal in equatorial SST anomaly propagation (9, 14), possibly due to altered background state (15–17). Whether the 2023 event signifies a resurgence of RC composite-type El Niño awaits confirmation through continued observations in the future. As the 2023 coastal warming after May is closely linked to basin-scale El Niño with relatively minor effects in the far eastern Pacific, hereafter, we focus on the atmospheric and oceanic dynamics during March–May.

Ocean dynamics

We first conduct a mixed layer heat budget analysis for the 2023 coastal El Niño to reveal the underlying physical processes. Figure S6A shows that the thermodynamical processes, particularly the shortwave radiation and latent heat flux (fig. S6E), primarily dampened the 2023 coastal El Niño during March–May. Figure S6A also highlights that vertical advection drives the coastal SST warming throughout March and April, with the Ekman feedback ($-w'T'_z$) dominating (fig. S6C). Specifically, the northerly alongshore wind anomalies strongly suppress upwelling in the coastal region (fig. S6D), thus raising CSA SST. This weakened upwelling coincided with record-low Chl-a since measurements began in 2002 (fig. S3). Moreover, the thermocline feedback ($-\bar{w}T'_z$) term is also important for coastal SST increase in April. After May, the thermocline feedback becomes dominant (fig. S6C), and the CSA warming is primarily caused by basin-scale wave dynamics. The meridional advection term is an additional positive contributor to the coastal warming during April–May. In the CSA region, the northerly wind anomalies drive anomalous southward currents (fig. S6D), resulting in warm advection along the coast.

Observations show that the 2023 coastal El Niño is accompanied by strong northerly alongshore wind anomalies in the southeastern

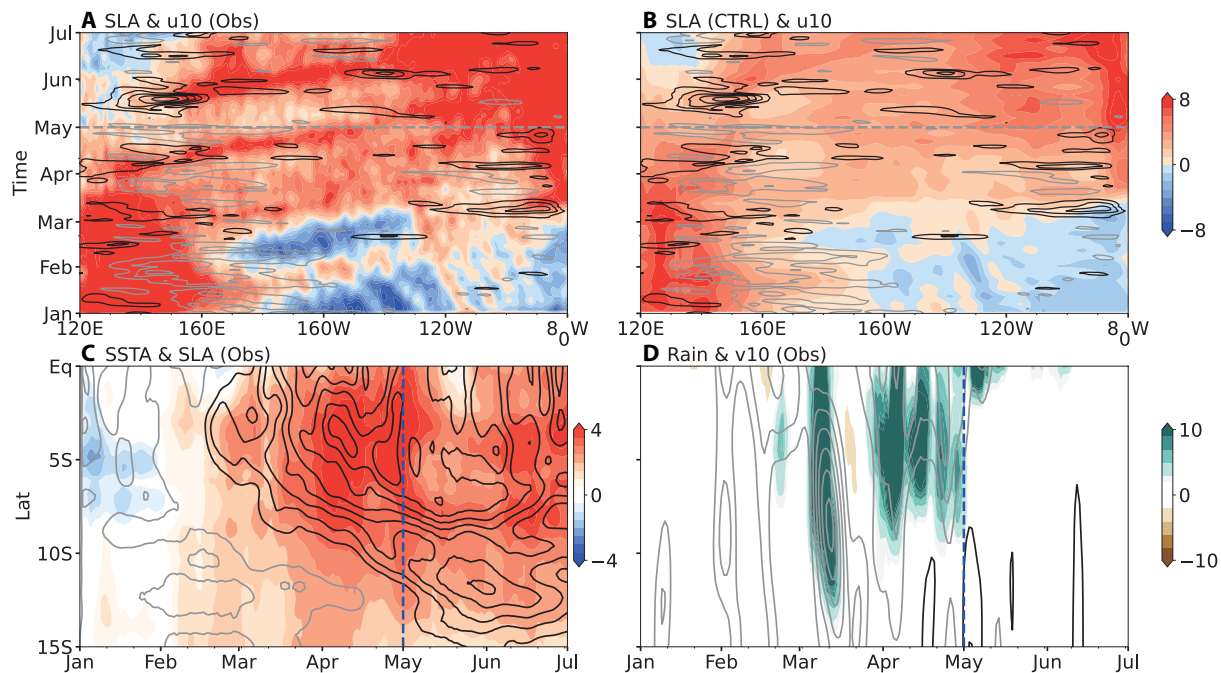


Fig. 2. Evolution of the 2023 coastal El Niño. Longitude-time Hovmöller diagram of u_{10} anomalies (line contours with an interval of 2 m/s; positive black and negative gray) as well as (A) observed SLA (cm, color shading) and (B) simulated SLA from the OGCM CTRL run (cm, color shading). All meridionally averaged over 2°S to 2°N. Latitude-time evolution of (C) SSTA (°C, color shading) and SLA (line contours with an interval of 2 cm; positive black and negative gray), and (D) rainfall (millimeters per day, color shading) and v_{10} anomalies (line contours with an interval of 1 m/s, positive black and negative gray) zonally averaged over 80°W to 85°W. The dashed line indicates the approximate time when the coastal rainfall and wind anomaly signals disappear.

Pacific and westerly (easterly) wind anomalies along the eastern (central and western) Pacific during February–April (Figs. 1 and 2A). We conduct three OGCM experiments denoted as τ'_{Coast} , τ'_{EEP} , and τ'_{WEP} to quantify the relative importance of wind anomalies over the coastal region, the EEP, and the central-western equatorial Pacific, respectively (see Materials and Methods). The control run (CTRL), a hindcast run forced by the full forcings (see Materials and Methods), captures the key characteristics of the 2023 coastal El Niño. Specifically, the simulated warming signals in the CTRL simulation are largely confined to the coastal regions during March–April (fig. S7), along with a weak La Niña state in the central Pacific, consistent with observations. The simulated CSA SSTA anomalies show that weak positive anomalies began in mid-February, followed by a rapid intensification during March and April. The anomalies reached their peak amplitude of approximately 4°C in late April and then decayed in May (Fig. 3A), similar to observations. In addition, the CTRL run successfully simulates the Kelvin waves, including the upwelling Kelvin waves in January and February and downwelling Kelvin waves from March to June (Fig. 2B). Overall, the good model/observation agreement provides confidence in the subsequent numerical experiments to examine key factors responsible for the 2023 coastal El Niño.

Figure 3B shows that the coastal wind stress anomalies dominate the 2023 coastal El Niño, contributing approximately +2.5°C SSTA warming. Specifically, the northerly alongshore wind anomalies strongly suppress the coastal upwelling and raise SSTA there, consistent with the heat budget results (fig. S6C). In addition, the coastal wind anomalies excite downwelling coastal Kelvin waves (Fig. 3B), which depress the thermocline off Peru and raise SSTA there. The simulated

CSA warming in τ'_{Coast} amplifies in March, peaks at the end of April, and declines in May due to the dissipation of the alongshore wind anomalies, much as in observations and the CTRL run.

The wind stress anomalies over the EEP (90°W to 130°W, 5°S to 5°N; τ'_{EEP}) cause sizable warming (~1.5°C) along the coast (Fig. 3C). These westerly wind anomalies drive downwelling equatorial Kelvin waves, which propagate eastward along the equatorial waveguide. Upon arriving at the east coast, the signals split to the south and then propagate along the coast of South America, leading to strong coastal warming through thermocline feedback in April–May. Our heat budget analysis also underscores the importance of the thermocline feedback in driving coastal warming during April, consistent with the results from the τ'_{EEP} experiment and confirming that the EEP westerly wind anomalies contribute to the coastal El Niño (10). Despite the weakening of the EEP westerly wind anomalies after May (Fig. 2A), the positive SSTA anomalies in the eastern Pacific persist (Fig. 3C). This persistence is likely due to the time lag associated with Kelvin wave propagation.

The central-western equatorial Pacific wind anomalies (τ'_{CWP}) have different impacts on the coastal El Niño. Before March, easterly wind anomalies prevail over the central-western Pacific (Fig. 2A), exciting weak upwelling Kelvin waves that cool SSTA along the coast (Fig. 3D). From March onward, a series of westerly wind bursts occur west of 160°E, driving equatorial downwelling Kelvin waves (Fig. 2A) (18, 19). It takes 3 months for these waves to propagate into the coastal region, contributing to the coastal warming after June (Fig. 3D). The dominant role of thermocline feedback arising from basin-scale wave dynamics after June is further confirmed by the heat budget analysis (fig. S6C). By this time, coastal

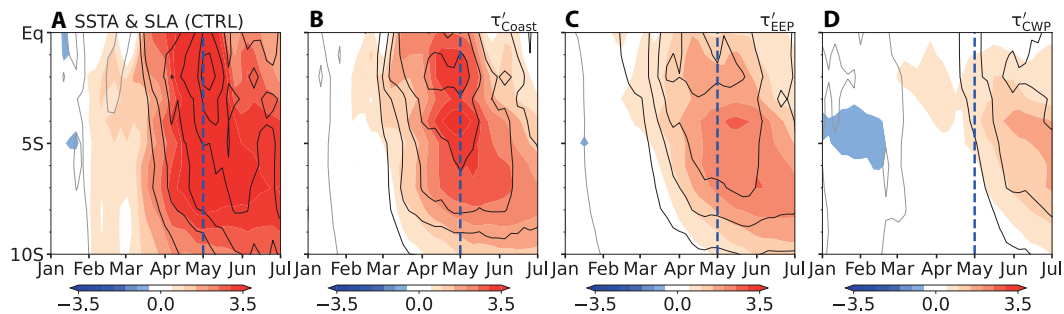


Fig. 3. Latitude-time evolution of the 2023 extreme coastal El Niño in OGCM experiments. Latitude-time Hovmöller diagrams of coastal (80°W to 85°W) SST anomalies (color shading; degree Celsius) and SLA (contours with an interval of 2 cm; positive black, zero omitted and negative gray) from the OGCM (A) CTRL, (B) τ_{Coast} , (C) τ_{EEP} , and (D) τ_{CWP} simulations.

warming is primarily due to the well-known basin-scale El Niño–Southern Oscillation (ENSO) dynamics (13, 20, 21), which differ from those growing the coastal El Niño. Thus, wind stress variations east of 130°W cause the coastal El Niño to grow, while wind anomalies to the west contribute to the persistence of the coastal warming after May. It has been widely accepted that the warming along the Peruvian coast during the onset of basin-scale El Niño is induced by remote forcings from the central Pacific (20). However, our results indicate that this perspective is not applicable when coastal El Niño occurs: In such cases, the coastal warming is primarily driven by local wind anomalies in the far eastern Pacific, with remote forcings playing a minimal role.

Atmospheric response and coastal Bjerknes feedback

To explore the atmospheric response to coastal warming, we performed a 10-member AGCM experiment (“AGlobal”) forced by globally observed SSTs (see Materials and Methods). The AGlobal ensemble mean, which averages out atmospheric internal variability, represents the atmospheric (e.g., precipitation and surface wind) responses induced by SST anomalies. The AGlobal experiment broadly captures observed atmospheric anomalies in the far southeastern Pacific during March and April, including deep convection (together with heavy rainfall) (Fig. 1, F and H), sizable westerly anomalies over the EEP, and strong alongshore northerly wind anomalies over the southeastern Pacific (Fig. 1, right). This indicates that a substantial portion of the atmospheric response is driven by the 2023 SST anomalies. To further isolate the impacts of the 2023 coastal warming, we conducted the “Acoast2023” experiment. In this experiment, observed SST anomalies are prescribed only over the CSA region, while the remaining ocean is set to its climatological values (see Materials and Methods). The Acoast2023 successfully reproduces key features for the 2023 event, including heavy rainfall off Peru, the strong northerly alongshore winds, and the deep meridional overturning cell in the far eastern Pacific with ascent/descent in the southern/northern hemisphere, closely resembling both the observations and the AGlobal experiment (figs. S8 and S9). Therefore, the atmospheric responses in the far eastern Pacific are predominantly driven by the 2023 coastal warming.

Together, the above OGCM and AGCM results imply positive feedback between the coastal warming and wind anomalies over the far eastern Pacific Ocean. Northerly (westerly) wind anomalies over the coastal (EEP) region cause anomalous coastal SST warming,

Once the coastal SSTs rise above the convective threshold, the convective anomalies cause a Matsuno-Gill response (22, 23) with anomalous northerly (westerly) winds over the coastal (EEP) region. These wind anomalies in turn intensify the coastal warming (6). In addition, the Intertropical Convergence Zone (ITCZ) and wind anomalies across the Pacific Ocean are coupled with basin-scale ENSO (24, 25). The preceding basin-scale La Niña could destabilize the ITCZ through reduced tropospheric stability (7) and positive feedback that strengthens (weakens) the ITCZ south (north) of the equator (6, 26, 27), favoring northerly coastal wind anomalies.

Unlike the equatorial Bjerknes feedback during basin-scale ENSO (28), the coastal Bjerknes feedback in this region operates within a specific time window: It is only active during February–March–April (FMA) and plays a crucial role in the phase-locking behavior of extreme coastal El Niño events. Specifically, during FMA when SSTs off Peru reach their annual maximum and are close to the convective threshold, coastal warming can cause deep convection and thus activate the coastal Bjerknes feedback. In other seasons, however, background SST is too low for deep convection south of the equator even with large coastal warming, which decouples the coastal warming and eastern Pacific wind anomalies. As a result, the extreme coastal El Niño peak phase is locked to FMA, in contrast to basin-scale El Niño. In 2023, the coastal Bjerknes feedback was active during March and April, manifested by strong wind and rainfall anomalies over the southeastern Pacific (Figs. 1 and 2). These strong atmospheric responses contrast with the considerably weak responses observed in this region within the RC composite. After May, this positive feedback became inactive due to the background SST cooling (fig. S4), explaining why the 2023 coastal El Niño and especially the atmospheric anomalies started to decay in May.

The activation of this coastal Bjerknes feedback is a key source of predictability of the 2023 coastal El Niño. At the end of February, the seasonal background warming, the suppressed upwelling, and the arrival of the first downwelling Kelvin wave pulse (Fig. 2A and fig. S4) work together to raise SSTs off Peru to exceed the convective threshold, activating the coastal Bjerknes feedback. Seasonal forecast models from the North American Multi-Model Ensemble (NMME) successfully captured this coastal Bjerknes feedback, which explains why the NMME started to predict heavy rainfall over the CSA region when initialized on 1 March and 1 April (fig. S10).

Role of atmospheric perturbations

SST-forced wind anomalies as in the AGlobal ensemble-mean last for a season or longer (fig. S11, I and J). Superimposed on these slow SST-forced wind variations are higher-frequency wind anomalies over the far eastern Pacific. In early March, a patch of strong westerly wind anomalies appeared over the EEP, mostly associated with the 30- to 90-day Madden–Julian Oscillation (MJO) (Fig. 4B and fig. S11E). The March 2023 MJO index was in phase 8 and the strongest since 1974 (Fig. 4A). A phase 8 MJO features westerly wind anomalies at 850 hPa in the EEP, with suppressed (active) convection over the maritime continent (South America). The band-pass (30 to 90 days) filtered results indicate that the phase 8 MJO event creates strong 10-m zonal wind (u_{10}) anomalies of ~ 2 m/s over the EEP and v_{10} anomalies of -1.5 m/s over the coastal region during the first half of March (fig. S11, E and F) (29). In addition, during 6 to 20 March 2023, a highly unusual tropical depression system dubbed “Cyclone Yaku” developed off Peru centered at $\sim 8^\circ\text{S}$ (fig. S12A). Such a cyclonic depression-like system is exceptionally rare there due to cool background SSTs. This low-pressure system induces 4.5 (3.7) m/s northerly alongshore (westerly) winds over the

coastal region (EEP) in mid-March (figs. S11, C and D, and S12A). The wind perturbations associated with the MJO and tropical depression system favor coastal warming by suppressing coastal upwelling and exciting downwelling Kelvin waves.

Yaku was accompanied by considerable rainfall so it is conceivable that eastern Pacific atmospheric variability such as Yaku could be energized by coastal warming and deep convection. We investigate this possibility by comparing the March–April ensemble SD (a measure of internal atmospheric variability) from AGlobal in 2023 with the climatological value during 2010–2022. In support of the hypothesis, Table 1 shows that the coastal warming in March–April 2023 strengthens the ensemble SD of rainfall and v_{10} in CSA by 123 and 64%, respectively, relative to their climatological values. The ACoast2023 experiment also yields similar results.

To explore what drives internal variability of alongshore winds off Peru, we have calculated the wind and precipitation regressions against the ensemble spread in CSA v_{10} during March–April 2023 in AGlobal. A Yaku-like cyclonic circulation off Peru emerges with increased rainfall near the center and westerly wind anomalies on the equator (fig. S13A, sign reversed). Ensemble member 10

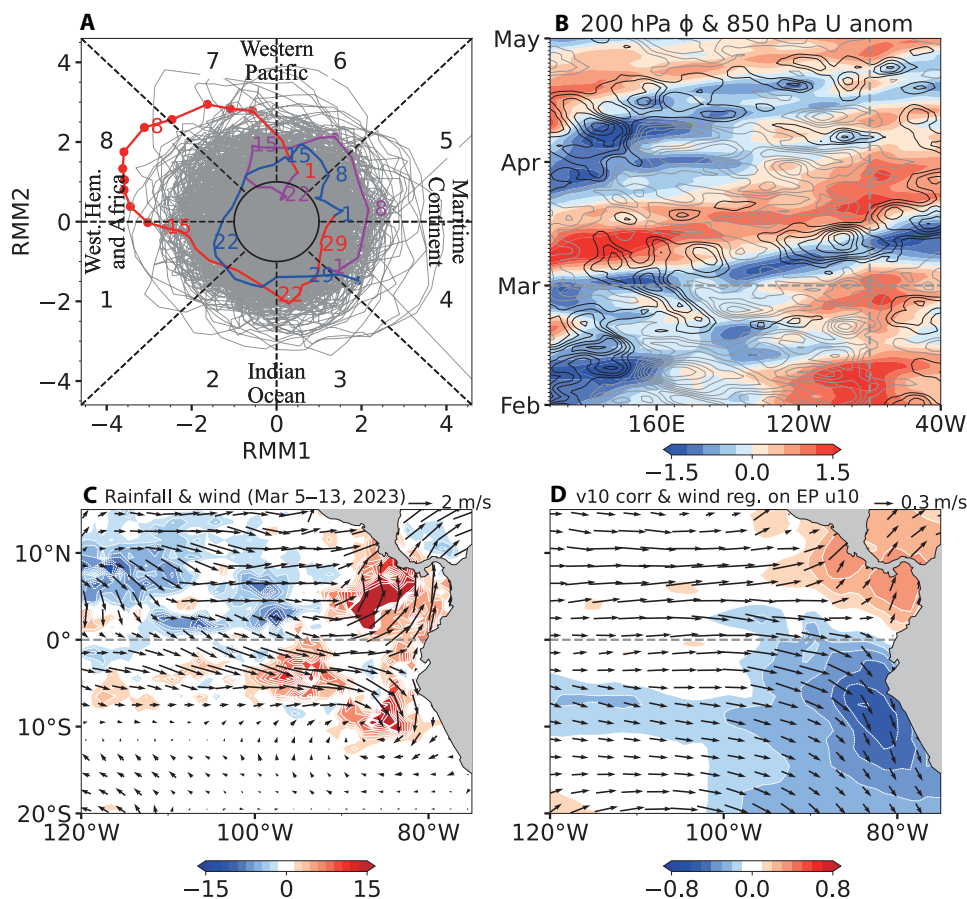


Fig. 4. Weather to intraseasonal timescale perturbations during the 2023 event. (A) The Wheeler-Hendon phase diagram for June 1974 to July 2023. The 2023 MJO index is highlighted in color, with February in magenta, March in red, and April in blue. (B) Hovmöller diagrams of equatorial (5°S to 5°N) 200 hPa velocity potential (ϕ , color shading, m^2/s) and 850-hPa zonal wind anomalies (line contours with an interval of 1 m/s; positive black and negative gray). (C) Observed 30 to 90 band-filtered anomalies of rainfall (millimeters per day; color shading) and 10-m wind (meters per second, vectors), averaged during 5 to 13 March 2023. (D) Correlation (color shading) of observed v_{10} with eastern Pacific (EP, 85°W to 100°W, 2°S to 2°N) averaged u_{10} ; also shown are 10-m wind regressions (vectors) onto EP u_{10} (30- to 90-day band-filtered anomalies used for 2012–2023).

Table 1. SD of ensemble spread in CSA v10, rainfall, and EP u10 in AGlobal experiments. Monthly anomalies are first calculated, followed by the computation of the SD from the squared variance averaged for March and April.

Variable	Climatological (2010–2022)	2023	Fractional difference
CSA v10	0.42	0.69	+64%
CSA rainfall	1.59	3.52	+123%
EP u10	0.78	1.08	+38%

produces a Yaku-like tropical depression off Peru (fig. S12B). The northerly wind anomalies off Peru act to strengthen the coastal warming. The regression against CSA v10 ensemble spread during 2010–2022 in AGlobal exhibits similar pattern, albeit with much-reduced magnitudes (not shown). This implies positive feedback between the coastal warming and internal atmospheric variability such as Yaku-like coastal tropical depression systems.

The topography of the Andes mountains is important in modulating ENSO variability (30). For the 2023 coastal El Niño, the record-strong phase 8 MJO during 5 to 13 March features broad westerly anomalies on the equator that impinge on the steep Andes mountains (Fig. 4C). At low levels, the orographic barrier forces poleward-propagating Kelvin waves with poleward flows west of the Andes. Cyclone Yaku develops on the cyclonic region of the topographically forced flow off Peru, aided by convective heating induced by coastal warming. Likewise, the intraseasonal easterly phase during the second half of February corresponds to a southerly surge off Peru at 10°S (fig. S11, E and F). A regression analysis for the 30- to 90-day observed EEP u10 during 2012–2023 confirms the funnel-like flow pattern off CSA (Fig. 4D and fig. S13B). Further research is necessary to investigate the connection between the MJO and v10 variability off Peru, as both are important forcings of coastal El Niño.

DISCUSSION

We have investigated the evolution and coupled mechanisms of the 2023 extreme coastal El Niño using observations and GCM experiments. In early March, a record-strong MJO drives westerly wind anomalies over the EEP, and a rare low-pressure system Yaku develops off Peru with anomalous northerly alongshore winds. Our OGCM and heat budget analysis results show that these anomalous winds are crucial in driving the 2023 coastal El Niño by suppressing coastal upwelling and deepening the thermocline depth via downwelling Kelvin waves (6, 10, 11).

The AGCM results further show that the SST warming drives deep convection south of the equator, strengthening the coastal northerly and EEP westerly anomalies. The intensified wind anomalies further amplify the coastal warming, indicative of coupled positive feedback. This coastal Bjerknes feedback is important in intensifying, sustaining, and predicting the 2023 coastal El Niño. In May, the background seasonal cooling inhibits deep convection and the coastal Bjerknes feedback, causing the coastal El Niño to decay. We further identify a positive feedback between coastal warming and internal atmospheric variability such as Yaku-like cyclones off Peru. Our analysis suggests that Yaku is part of the strong phase 8 MJO, induced by the orographic effect of the high Andes and

amplified by convective heating over warm coastal waters. Given the rarity of extreme coastal El Niño, the 2023 case provides a valuable opportunity to test ocean-atmospheric processes involved.

Coastal SST off Peru has exhibited a warming trend since the mid-2010s (fig. S2), possibly related to the fact that the two most extreme coastal El Niño events since 1925 both occurred after 2017. The increase in the frequency and intensity of coastal El Niño took place despite a La Niña-like pattern of SST change over the recent three decades. Anthropogenic global warming (31) is likely to affect the characteristics of coastal El Niño events. The El Niño-like warming pattern projected by climate models reduces the barrier to deep convection and strengthens the coastal Bjerknes feedback off Peru and Ecuador, favoring increased frequency and intensity of extreme coastal El Niño events (6). With more frequent occurrences of coastal El Niño, the compounded heavy rainfall would result in greater damages in a warmer climate.

MATERIALS AND METHODS

Observational and reanalysis datasets

We used the daily and monthly National Oceanic and Atmospheric Administration (NOAA) Optimum Interpolation Sea Surface Temperature version 2 dataset (OISSTv2) during 1982–2023 (32), daily wind velocity derived from the Cross-Calibrated Multi-Platform Version 2.0 (CCMP V2.0) from Remote Sensing Systems (33), and daily SLA from the Copernicus Marine and Environment Monitoring Service (CMEMS). All datasets mentioned above are at $0.25^\circ \times 0.25^\circ$ resolution. The daily air-sea fluxes are derived from the ERA5 reanalysis data (34). We used the daily $0.1^\circ \times 0.1^\circ$ precipitation spanning 2001–2023 from the Global Precipitation Measurement (GPM) (35) and monthly $2.5^\circ \times 2.5^\circ$ rainfall from Global Precipitation Climatology Project (GPCP) during 1979–2023 (36). Before the analysis, we eliminated the long-term trend within these datasets. The ocean temperature, mixed layer depth, currents, and monthly SLA are obtained from the National Centers for Environmental Prediction (NCEP) Global Ocean Data Assimilation System. The Real-time Multivariate MJO indices (RMM1 and RMM2) are used to track the MJO activities. We also use monthly $0.1^\circ \times 0.1^\circ$ MODIS Chl-a concentration data (37) to investigate the marine ecological response. The in situ coastal SST data are obtained from the Instituto del Mar del Peru.

OGCM experiments

We used the MIT General Circulation Model (MITgcm) in this study. The model is configured to a Lat-Lon-Cap (LLC270) grid, with a horizontal resolution of $1/3^\circ$ in the zonal direction and $1/9^\circ$ in the meridional direction at low and high latitudes, stretching to

1/3° at mid-latitudes. The model has 50 vertical layers, with layer thickness gradually increasing from 5 m near the surface to 456 m in the deep ocean. The diffusion and mixing parameters of the model are identical to those used in previous studies (38, 39). In the hind-cast run (hereafter CTRL), the MITgcm was integrated forward in time from 1 January 2000 to 1 July 2023, forced by 6-hourly realistic wind stress, wind speed, downward shortwave and longwave radiations, precipitation, and 2-m air temperature and humidity from the JRA55-do product (40).

As thermodynamics primarily act to damp the 2023 coastal El Niño (figs. S6A and S6C), here, we mainly focus on the underlying dynamic process forced by anomalous wind stress. To investigate the relative importance of wind stress anomalies over the coastal region (75°W to 90°W, 20°S to 5°N), the EEP (90°W- to 130°W, 5°S to 5°N) and the central-western Pacific Ocean (CWP; 120°E to 130°W, 5°S to 5°N), we conduct three sensitive experiments (table S1). In the coastal wind run (τ'_{Coast}), we retained time-varying wind stress over the coastal region but daily climatological wind stress outside this region with a 3° buffer region where the strength of the wind stress anomalies is linearly reduced, and all the other forcings are fixed to their daily climatological values. The EEP (τ'_{EEP}) [central-western Pacific wind run (τ'_{CWP})] is similar to the τ'_{Coast} except that only the time-varying wind stress in the eastern (central-western) equatorial Pacific is retained. The solutions, τ'_{Coast} , τ'_{EEP} , and τ'_{CWP} , thus isolate the dynamic effects of wind stress anomalies over the coastal region, EEP, and CWP, respectively.

AGCM experiments

To evaluate the effects of coastal warming, we performed two experiments. In the AGlobal run, we force the Geophysical Fluid Dynamics Laboratory AM4.0 (41) with 1/4° observed daily OISST (42) from 1 January 2010 to 30 June 2023. The model resolution is approximately 100 km with 33 levels in the vertical. The AGlobal is radiatively forced by historical (until 2014) and Shared Socio-economic Pathway 2-4.5 scenarios in Coupled Model Intercomparison Project phase 6 (43). The AGlobal experiments have 10 members, each with slightly different initial conditions. The ensemble mean of the simulations is analyzed to assess the atmospheric response to 2023 SST anomalies across the global ocean, and the spread (SD) indicates the uncertainty from internal variability, prominently reflecting the influence of MJO and weather-scale perturbation in tropical regions. The coastal run (ACoast2023) is similar to AGlobal; however, starting from 1 January 2023, it retains only realistic SST in the coastal region (90°W-coast, 15°S-equator, with 5° linear tapering zones outside this region) while using climatological SST in other regions. The results thus isolate the atmospheric responses to 2023 coastal SST anomalies.

Ocean mixed layer heat budget

Here, we use a mixed layer heat budget (26) to assess the relative contribution of ocean dynamics and thermodynamics to the 2023 coastal El Niño.

$$T'_t = -(uT'_x)' - (vT'_y)' - (wT'_z)' + \left(\frac{Q_{\text{net}} - Q_{\text{pen}}}{\rho c_p H} \right)' + R \quad (1)$$

where u , v , and T indicate the mixed layer averaged zonal current, meridional current, and ocean temperature, respectively. w is the vertical velocity at the bottom of the mixed layer. The Q_{net} is the

surface net heat flux, and the Q_{pen} is the shortwave radiation transmitted through the bottom of the mixed layer depth. ρ and c_p are the density and specific heat capacity of seawater, respectively; and H is the mean mixed layer depth (here we use the monthly climatological mixed layer depth). R is the residual term. The vertical advection term $[-(wT'_z)']$ could be further decomposed into the thermocline feedback ($-\overline{wT'_z}$), the Ekman feedback ($-\overline{w'T'_z}$), and the nonlinear term ($-\overline{w'T'_z}$). Here, the overbar indicates the climatological value, and the prime indicates the anomalies. More details can be found in (26).

Supplementary Materials

This PDF file includes:

Table S1

Figs. S1 to S13

REFERENCES AND NOTES

1. P. Rau, L. Bourrel, D. Labat, P. Melo, B. Dewitte, F. Frappart, W. Lavado, O. Felipe, Regionalization of rainfall over the Peruvian Pacific slope and coast. *Int. J. Climatol.* **37**, 143–158 (2017).
2. S. Bagchi, Dengue outbreak in Peru affects adults and children. *Lancet Infect. Dis.* **23**, e339 (2023).
3. C. Cabezas Sánchez, Dengue in Peru: chronicle of recurrent epidemics (1990–2023), the virus, *Aedes aegypti* and determinants, where are we going? *An. Fac. Med.* **84**, 145–148 (2023).
4. Comité Multisectorial Encargado del Estudio Nacional del Fenómeno El Niño (ENFEN), Informe Técnico ENFEN. Año 9, 7, 58 (2023).
5. C. Deser, J. M. Wallace, El Niño events and their relation to the Southern Oscillation: 1925–1986. *J. Geophys. Res. Oceans* **92**, 14189–14196 (1987).
6. Q. H. Peng, S. P. Xie, D. X. Wang, X. T. Zheng, H. Zhang, Coupled ocean-atmosphere dynamics of the 2017 extreme coastal El Niño. *Nat. Commun.* **10**, 298 (2019).
7. K. Takahashi, A. G. Martínez, The very strong coastal El Niño in 1925 in the far-eastern Pacific. *Clim. Dyn.* **52**, 7389–7415 (2019).
8. R. D. Garreaud, A plausible atmospheric trigger for the 2017 coastal El Niño. *Int. J. Climatol.* **38**, e1296–e1302 (2018).
9. Z. Z. Hu, B. H. Huang, J. S. Zhu, A. Kumar, M. J. McPhaden, On the variety of coastal El Niño events. *Clim. Dyn.* **52**, 7537–7552 (2019).
10. S. Zhao, C. Karaperidou, Competing effects of Eastern and Central-Western Pacific winds in the evolution of the 2017 extreme coastal El Niño. *Geophys. Res. Lett.* **49**, e2022GL098859 (2022).
11. V. Echevin, F. Colas, D. Espinoza-Morriberon, L. Vasquez, T. Anculle, D. Gutierrez, Forcings and evolution of the 2017 coastal El Niño off northern Peru and Ecuador. *Front. Mar. Sci.* **5**, 367 (2018).
12. C. Rodríguez-Morata, H. Díaz, J. Ballesteros-Canovas, M. Rohrer, M. Stoffel, The anomalous 2017 coastal El Niño event in Peru. *Clim. Dyn.* **52**, 5605–5622 (2019).
13. E. M. Rasmusson, T. H. Carpenter, Variations in tropical Sea Surface temperature and surface wind fields associated with the Southern Oscillation/El Niño. *Mon. Weather Rev.* **110**, 354–384 (1982).
14. M. J. McPhaden, X. Zhang, Asymmetry in zonal phase propagation of ENSO sea surface temperature anomalies. *Geophys. Res. Lett.* **36**, 245–257 (2009).
15. A. V. Fedorov, S. G. Philander, A stability analysis of tropical ocean-atmosphere interactions: Bridging measurements and theory for El Niño. *J. Climate* **14**, 3086–3101 (2001).
16. Z.-Z. Hu, A. Kumar, B. Huang, J. Zhu, M. L'Heureux, M. J. McPhaden, J.-Y. Yu, The interdecadal shift of ENSO properties in 1999/2000: A review. *J. Climate* **33**, 4441–4462 (2020).
17. B. Wang, S. An, A mechanism for decadal changes of ENSO behavior: Roles of background wind changes. *Clim. Dyn.* **18**, 475–486 (2002).
18. S. Hu, A. V. Fedorov, The extreme El Niño of 2015–2016: The role of westerly and easterly wind bursts, and preconditioning by the failed 2014 event. *Clim. Dyn.* **52**, 7339–7357 (2019).
19. Y. Liang, A. V. Fedorov, Linking the Madden-Julian Oscillation, tropical cyclones and westerly wind bursts as part of El Niño development. *Clim. Dyn.* **57**, 1039–1060 (2021).
20. K. Wyrtki, El Niño—the dynamic response of the equatorial Pacific Ocean to atmospheric forcing. *J. Phys. Oceanogr.* **5**, 572–584 (1975).
21. K. Takahashi, A. Montecinos, K. Goubanova, B. Dewitte, ENSO regimes: Reinterpreting the canonical and Modoki El Niño. *Geophys. Res. Lett.* **38**, L10704 (2011).

22. A. E. Gill, Some simple solutions for heat-induced tropical circulation. *Q. J. R. Meteorol. Soc.* **106**, 447–462 (1980).
23. T. Matsuno, Quasi-geostrophic motions in the equatorial area. *J. Meteorol. Soc. Japan Ser.* **44**, 25–43 (1966).
24. J. C. Chiang, A. H. Sobel, Tropical tropospheric temperature variations caused by ENSO and their influence on the remote tropical climate. *J. Climate* **15**, 2616–2631 (2002).
25. G. A. Vecchi, The termination of the 1997–98 El Niño. Part II: Mechanisms of atmospheric change. *J. Climate* **19**, 2647–2664 (2006).
26. Q. H. Peng, S. P. Xie, D. X. Wang, Y. C. Kamae, H. Zhang, S. N. Hu, X. T. Zheng, W. Q. Wang, Eastern Pacific wind effect on the evolution of El Niño: Implications for ENSO diversity. *J. Climate* **33**, 3197–3212 (2020).
27. S. P. Xie, Q. H. Peng, Y. Kamae, X. T. Zheng, H. Tokinaga, D. X. Wang, Eastern Pacific ITCZ dipole and ENSO diversity. *J. Climate* **31**, 4449–4462 (2018).
28. J. Bjerknes, Atmospheric teleconnections from the equatorial PACIFIC1. *Mon. Weather Rev.* **97**, 163–172 (1969).
29. D. Waliser, K. Sperber, H. Hendon, D. Kim, M. Wheeler, K. Weickmann, C. Zhang, L. Donner, J. Gottschalck, W. Higgins, I. S. Kang, D. Legler, M. Moncrieff, F. Vitart, B. Wang, W. Wang, S. Woolnough, E. Maloney, S. Schubert, W. Stern, C. M.-J. Oscillation, MJO Simulation Diagnostics. *J. Clim.* **22**, 3006–3030 (2009).
30. W. Xu, J.-E. Lee, B. Fox-Kemper, Y. Planton, M. J. McPhaden, The andes affect ENSO statistics. *J. Climate* **35**, 7077–7091 (2022).
31. W. Cai, B. Ng, T. Geng, F. Jia, L. Wu, G. Wang, Y. Liu, B. Gan, K. Yang, A. Santoso, Anthropogenic impacts on twentieth-century ENSO variability changes. *Nat. Rev. Earth Environ.* **4**, 407–418 (2023).
32. R. W. Reynolds, N. A. Rayner, T. M. Smith, D. C. Stokes, W. Q. Wang, An improved in situ and satellite SST analysis for climate. *J. Climate* **15**, 1609–1625 (2002).
33. C. Mears, T. Lee, L. Ricciardulli, X. Wang, F. Wentz, Improving the accuracy of the Cross-Calibrated Multi-Platform (CCMP) ocean vector winds. *Remote Sens. (Basel)* **14**, 4230 (2022).
34. H. Hersbach, B. Bell, P. Berrisford, S. Hirahara, A. Horanyi, J. Muñoz-Sabater, J. Nicolas, C. Peubey, R. Radu, D. Schepers, A. Simmons, C. Soci, S. Abdalla, X. Abellan, G. Balsamo, P. Bechtold, G. Biavati, J. Bidlot, M. Bonavita, G. De Chiara, P. Dahlgren, D. Dee, M. Diamantakis, R. Dragani, J. Flemming, R. Forbes, M. Fuentes, A. Geer, L. Haimberger, S. Healy, R. J. Hogan, E. Holm, M. Janiskova, S. Keeley, P. Laloyaux, P. Lopez, C. Lupu, G. Radnoti, P. de Rosnay, I. Rozum, F. Vamborg, S. Villaume, J. N. Thepaut, The ERA5 global reanalysis. *Q. J. R. Meteorol. Soc.* **146**, 1999–2049 (2020).
35. G. Skofronick-Jackson, W. A. Petersen, W. Berg, C. Kidd, E. F. Stocker, D. B. Kirschbaum, R. Kakar, S. A. Braun, G. J. Huffman, T. Iguchi, P. E. Kirstetter, C. Kummerow, R. Meneghini, R. Oki, W. S. Olson, Y. N. Takayabu, K. Furukawa, T. Wilhelm, The Global precipitation measurement (Gpm) mission for science and society. *Bull. Am. Meteorol. Soc.* **98**, 1679–1695 (2017).
36. R. F. Adler, G. J. Huffman, A. Chang, R. Ferraro, P. P. Xie, J. Janowiak, B. Rudolf, U. Schneider, S. Curtis, D. Bolvin, A. Gruber, J. Susskind, P. Arkin, E. Nelkin, The version-2 global precipitation climatology project (GPCP) monthly precipitation analysis (1979–present). *J. Hydrometeorol.* **4**, 1147–1167 (2003).
37. W. E. Esaias, M. R. Abbott, I. Barton, O. B. Brown, J. W. Campbell, K. L. Carder, D. K. Clark, R. H. Evans, F. E. Hoge, H. R. Gordon, W. M. Balch, R. Letelier, P. J. Minnett, An overview of MODIS capabilities for ocean science observations. *IEEE Trans. Geosci.* **36**, 1250–1265 (1998).
38. Q. Peng, S.-P. Xie, R. X. Huang, W. Wang, T. Zu, D. Wang, Indonesian throughflow slowdown under global warming: Remote AMOC effect versus regional surface forcing. *J. Climate* **36**, 1301–1318 (2023).
39. Q. Peng, S.-P. Xie, D. Wang, R. X. Huang, G. Chen, Y. Shu, J.-R. Shi, W. Liu, Surface warming-induced global acceleration of upper ocean currents. *Sci. Adv.* **8**, eabj8394 (2022).
40. H. Tsujino, L. S. Urakawa, S. M. Griffies, G. Danabasoglu, A. J. Adcroft, A. E. Amaral, T. Arsouze, M. Bentsen, R. Bernardello, C. W. Boning, A. Bozec, E. P. Chassignet, S. Danilov, R. Dussin, E. Exarchou, P. G. Fogli, B. Fox-Kemper, C. C. Guo, M. Ilicak, D. Iovino, W. M. Kim, N. Koldunov, V. Lapin, Y. W. Li, P. F. Lin, K. Lindsay, H. L. Liu, M. C. Long, Y. Komuro, S. J. Marsland, S. Masina, A. Nummelin, J. K. Rieck, Y. Ruprich-Robert, M. Scheinert, V. Sicardi, D. Sidorenko, T. Suzuki, H. Tatebe, Q. Wang, S. G. Yeager, Z. P. Yu, Evaluation of global ocean-sea-ice model simulations based on the experimental protocols of the Ocean Model Intercomparison Project phase 2 (OMIP-2). *Geosci. Model Dev.* **13**, 3643–3708 (2020).
41. M. Zhao, J. C. Golaz, I. Held, H. Guo, V. Balaji, R. Benson, J. H. Chen, X. Chen, L. Donner, J. Dunne, The GFDL global atmosphere and land model AM4.0/LM4.0: 1. Simulation characteristics with prescribed SSTs. *J. Adv. Model Earth Syst.* **10**, 691–734 (2018).
42. B. Huang, C. Liu, V. Banzon, E. Freeman, G. Graham, B. Hankins, T. Smith, H.-M. Zhang, Improvements of the daily optimum interpolation sea surface temperature (DOISST) version 2.1. *J. Climate* **34**, 2923–2939 (2021).
43. V. Eyring, S. Bony, G. A. Meehl, C. A. Senior, B. Stevens, R. J. Stouffer, K. E. Taylor, Overview of the coupled model intercomparison project Phase 6 (CMIP6) experimental design and organization. *Geosci. Model Dev.* **9**, 1937–1958 (2016).

Acknowledgments: We extend our gratitude to J.M. Wallace for engaging in insightful discussions. We thank the reviewers for constructive comments and suggestions, which improved the study. In addition, we would like to acknowledge the high-performance computing support provided by Cheyenne. **Funding:** Q.P. and S.-P.X. are supported by the National Science Foundation (AGS 1637450). S.-P.X. is additionally supported by NASA (80NSSC24M0010). A.M. is supported in part by the Japanese Ministry of Education, Culture, Sports, Science and Technology (MEXT) programs for the advanced studies of climate change projection (JPMXD0722680395). The National Center for Atmospheric Research (NCAR) is sponsored by the National Science Foundation under Cooperative Agreement 1852977. **Author contributions:** Q.P., S.-P.X., and G. A. P. designed the study. Q.P. conducted the analysis and OGCM experiments. A.M. designed and conducted the AGCM experiments. Q.P. and S.-P.X. wrote the paper with inputs from all the authors. Q.P., S.-P.X., C. D., G.A.P., and A.M. reviewed and edited the manuscript. **Competing interests:** The authors declare that they have no competing interests. **Data and materials availability:** The OISSTv2 dataset is available at <https://psl.noaa.gov/data/gridded/data.noaa.oisst.v2.highres.html>; CCMP V2.0 at <https://remss.com/measurements/ccmp>; CMEMS SLA at <https://marine.copernicus.eu/access-data>; ERA5 reanalysis data at <https://copernicus.eu/en>; GPM at https://disc.gsfc.nasa.gov/datasets/GPM_3IMERGDL_06/summary?keywords=GPM; GODAS at <https://esrl.noaa.gov/psd/data/gridded/data.godas.html>; GPCP at <https://psl.noaa.gov/data/gridded/data.gpcp.html>; the real-time MJO index at <http://bom.gov.au/climate/mjo/graphics/rmm.74toRealtime.txt>; the MODIS Chl-a concentration data at <https://earthdata.nasa.gov/>; the in situ SST data at http://imarpe.gob.pe/imarpe/index2.php?id_section=101780302000000000000000; the MITgcm and AM4.0 outputs at <https://zenodo.org/records/10437145>. All other data needed to evaluate the conclusions in this paper are present in the paper and/or the Supplementary Materials.

Submitted 16 September 2023

Accepted 15 February 2024

Published 22 March 2024

10.1126/sciadv.adk8646